Dalton Transactions



PAPER

View Article Online



Cite this: *Dalton Trans.*, 2025, **54**, 13588

Received 16th July 2025, Accepted 14th August 2025 DOI: 10.1039/d5dt01676b

rsc.li/dalton

Mixed-anion chalcogenide-halide semiconductors A_2BaTaS_4Cl (A = K, Rb, Cs) and K_2BaNbS_4Cl

Thomas S. Ie, D^a Siddhartha S. Nathan, D^b James M. Rondinelli D^b and Mercouri G. Kanatzidis D*^a

Four mixed-anion materials, K_2BaTaS_4Cl , Rb_2BaTaS_4Cl , Cs_2BaTaS_4Cl and K_2BaNbS_4Cl were synthesized via low temperature solid state synthesis at 848 K. All materials degrade upon melting to a mixture of the binary ionic salts, ACl, and ABaMS₄, two of which (KBaTaS₄ and CsBaTaS₄) are reported here for the first time. Single crystal X-ray diffraction revealed that K_2BaTaS_4Cl , Rb_2BaTaS_4Cl , and K_2BaNbS_4Cl crystallize in the tetragonal space group I4/mcm, adopting the Cs_3CoCl_5 structure type. In this phase, isolated $[MS_4]^{3-}$ tetrahedra are encapsulated within a (K, Rb)/Ba-Cl ionic cage. Although structurally similar, Cs_2BaTaS_4Cl crystallizes in the orthorhombic space group Ibam, arising from a supercell with a $\sqrt{2}$ expansion along the a-axis and a $2\sqrt{2}$ expansion along the b-axis due to extended Cs and Ba ordering. Consistent with electronic structure calculations, the measured bandgaps of the Ta-based compounds are ~ 3.0 eV while the Nb-based compounds exhibit a reduced bandgap of ~ 2.5 eV, reflecting the lower energy of the Nb d orbitals

1. Introduction

Mixed-anion or heteroanionic compounds, materials that contain more than one type of anion within a single structure, with each anion exhibiting some degree of long-range ordering, represent a particularly promising class of materials. The presence of multiple distinct anions enables access to properties that are typically unattainable in single-anion systems. 1-8 These properties include tunable bandgaps and crystal field splitting, reduced dimensionality, disrupted local symmetry, and enhanced structural diversity arising from unique bonding motifs enabled by the inclusion of multiple anionic species.3-11 Owing to these characteristics, heteroanionic materials have attracted interest across a wide range of research fields, including thermoelectrics, photocatalysis, and nonlinear optics. 4,9,12-15 The presence of multiple anions, however, also complicates the synthesis of novel heteroanionic compounds. 8,16 Although the number of potential compounds should theoretically increase exponentially, only a limited number have been reported to date. Consequently, the discovery of new heteroanionic materials often relies on more targeted approaches, such as compositional tuning within known compound families.

One particularly promising family for such tuning is Ba_3MQ_4X (M = Fe, Al, Ga, In; Q = S, Se; X = Cl, Br, I). These compounds exhibit significant structural flexibility, owing to their ability to accommodate various combinations of metals, chalcogens, and halides.¹⁷ Depending on the specific elemental radius ratios, members of this family can adopt several distinct structure types, including the Ba₃GaS₄Cl-type structure $(Pnma),^{17-21}$ the Cs₃CoCl₅/K₃SO₄F-type structure mcm), 17,19,22 or in the case of Ba₃GaS₄I, a unique structure type (Cmcm).23 Further compositional tuning has even been achieved by substituting Ba²⁺ with a monovalent alkali metal, allowing for the design of new compounds with tetravalent metals such as Ge or Sn, resulting in the general formula ABa_2MQ_4X (A = Na, K, Rb, Cs; M = Ge, Sn; Q = S, Se; X = Cl, Br, I). 24,25 This substitution not only expands the range of accessible materials but also allows for structural tuning based on the size of the alkali cation. This trend is illustrated in the ABa₂SnS₄X (A = Na, K, Rb, Cs) system. NaBa₂SnS₄Cl and KBa₂SnS₄Cl crystallize in the aforementioned Cs₃CoCl₅/ K₃SO₄F-type structure type. However, as the size of the alkali metal increases, RbBa2SnS4Cl and CsBa2SnS4Cl adopt a distorted structure due to changes in the Rb/Cs and Ba coordination environments, resulting in a monoclinic $P2_1/c$ space group. 24,26

Building on these findings, a logical extension involves substituting a second $\mathrm{Ba^{2+}}$ ion with a monovalent alkali metal, thereby enabling the stabilization of compounds containing pentavalent metals such as V, Nb, or Ta. This approach can be generalized using the composition $\mathrm{A_xBa_{3-x}M^{III+x}Q_4X}$, encom-

^aDepartment of Chemistry, Northwestern University, Evanston, IL 60208, USA. E-mail: m-kanatzidis@northwestern.edu

^bDepartment of Materials Science and Engineering, Northwestern University, Evanston, Illinois 60208, USA

Dalton Transactions Paper

passing a wide range of potential combinations. In this work, we demonstrate the feasibility of this strategy through the synthesis of four new mixed-anion materials, A₂BaTaS₄Cl (A = K, Rb, Cs) and K2BaNbS4Cl, as well as two additional singleanion compounds, ABaTaS₄ (A = K, Cs). We report their synthesis and characterization, focusing on phase stability, optical responses, and crystal structures, and how variations in the alkali metal component influence these properties.

Experimental section 2.

Synthesis 2.1.

Bulk A2Ba(Nb,Ta)S4Cl were synthesized at a 2 g scale by combining A₂S_r, BaS, ACl, Nb/Ta, and S in a stoichiometric ratio. Materials were homogenized using a mortar and pestle while inside an N2-filled glovebox and subsequently charged into an aluminum-lined carbon-coated fused silica tube (12.7 mm OD, 10.5 mm ID). All tubes were lined with aluminum foil to minimize powder-coating the inside walls of the tubes. The foil liner was then removed, and the tubes were taken from the glovebox and evacuated on a vacuum line to $\sim 3 \times 10^{-3}$ mbar. The tubes were subsequently flame-sealed using an oxygenmethane torch. The sealed tube was placed inside a one-zone programmable tube furnace packed with insulation wool. The furnace was heated to 575 °C at a rate of \sim 45 °C h^{-1} and left to dwell for 24 hours. The furnace was then cooled to room temperature at a rate of 10 °C h⁻¹. All tubes were opened inside an N₂-filled glovebox showing orange-yellow powders for all compounds. The ingots were then ground into powders and then washed using anhydrous dimethylformamide (DMF) to remove excess A2Sx resulting in a whitish yellow powder for K₂BaTaS₄Cl, Rb₂BaTaS₄Cl, and Cs₂BaTaS₄Cl and bright yellow powder for K₂BaNbS₄Cl. PXRD on all materials confirmed the phase formation alongside minor secondary phases for each compound (Fig. 1).

2.2. Single crystal growth

Single crystals of A₂BaMS₄Cl and ABaTaS₄ were synthesized at a 1 g scale by combining A₂S_x, BaS, ACl, Ta/Nb, and S in stoichiometric ratios. Materials were homogenized using a mortar and pestle while inside an N2-filled glovebox and subsequently charged into an aluminum-lined carbon coated fused silica tube (9 mm OD, 7 mm ID). All tubes were lined with aluminum foil to minimize powder-coating the inside walls of the tubes. The foil liner was then removed, and the tubes were taken from the glovebox and evacuated on a vacuum line to ~3 \times 10⁻³ mbar. The tubes were subsequently flame-sealed using an oxygen-methane torch. The sealed tube was placed inside a one-zone programmable tube furnace packed with insulation wool. The furnace was heated to 750 °C at a rate of ~60 °C h⁻¹ and left to dwell for 24 hours. The furnace was then cooled to room temperature at a rate of 10 °C h⁻¹. All tubes were opened inside an N2-filled glovebox showing yellow to clear single crystals for all samples. Powder X-ray Diffraction (PXRD) and single crystal analysis revealed products to be a mix of A₂BaTaS₄Cl, ABaTaS₄, and ACl (A = K, Rb, Cs) (Table 1 and Tables S1-7). Single crystals were then isolated from reaction without washing.

2.3. Single crystal X-ray diffraction (SCXRD)

For the acquisition of intensity data, suitable single crystals were mounted on a loop with paratone oil and mounted onto a XtaLAB Synergy Diffractometer. The XtaLAB Synergy diffractometer was equipped with a microfocus-sealed X-ray tube PhotonJet (Mo) X-ray source and a Hybrid Pixel Array Detector (HyPix). The temperature of the crystals was controlled with an Oxford Cryosystems 700 series low-temperature device. Data reduction was performed with the CrysAlisPro software (Rigaku) using an empirical and numerical absorption correction. All structures were solved with the ShelXT²⁷ structure solution program using the intrinsic phasing solution method

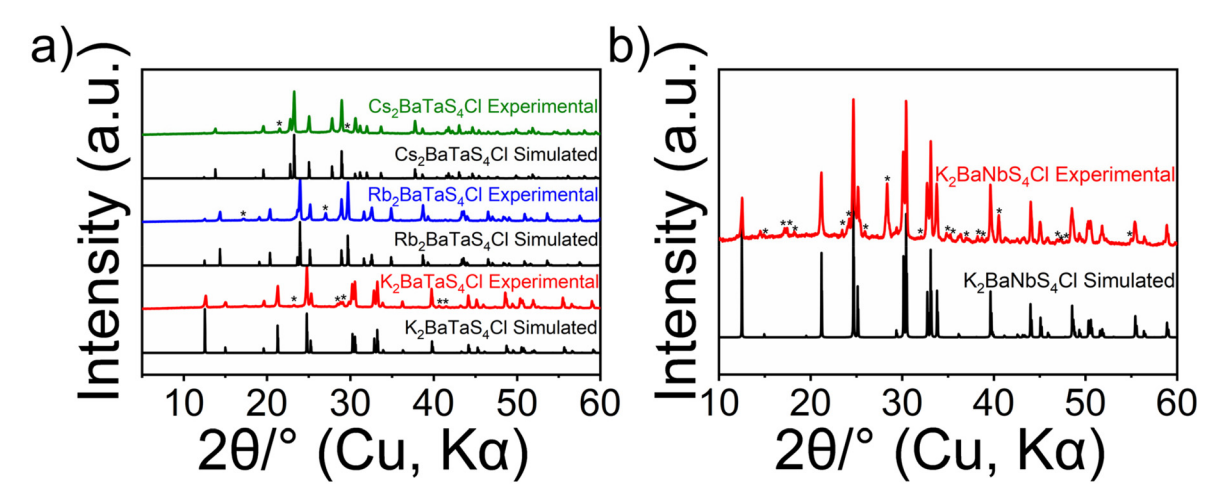


Fig. 1 PXRDs of (a) K₂BaTaS₄Cl, Rb₂BaTaS₄Cl, and Cs₂BaTaS₄Cl and (b) K₂BaNbS₄Cl when compared to their simulated patterns. Secondary phases are highlighted using stars, which are primarily composed of the alkali metal salts (KCl, RbCl, CsCl) and their single anion counterparts ABaMS₄ (A = K, Rb, Cs; M = Nb, Ta).

Table 1 Crystallographic data and structure refinement of K_2BaNbS_4Cl and A_2BaTaS_4Cl (A = K, Rb, Cs)

-				
Empirical formula	K ₂ BaNbS ₄ Cl	K_2BaTaS_4Cl	Rb₂BaTaS₄Cl	Cs ₂ BaTaS ₄ Cl
Formula weight	472.14	560.18	652.92	747.80
Temperature	278.5(7) K	297.15(10) K	275(1) K	101(2) K
Wavelength	0.71073 Å	0.71073 Å	0.71073 Å	0.71073 Å
Crystal system	Tetragonal	Tetragonal	Tetragonal	Orthorhombic
Space group	I4/mcm	I4/mcm	I4/mcm	Ibam
Unit cell dimensions	$a = 8.3800(2) \text{ Å}, \alpha = 90^{\circ}$	$a = 8.3480(2) \text{ Å}, \alpha = 90^{\circ}$	$a = 8.7216(2) \text{ Å}, \alpha = 90^{\circ}$	$a = 12.7216(2) \text{ Å}, \alpha = 90^{\circ}$
	$b = 8.3800(2) \text{ Å}, \beta = 90^{\circ}$	$b = 8.3480(2) \text{ Å, } \beta = 90^{\circ}$	$b = 8.7216(2) \text{ Å. } \beta = 90^{\circ}$	$b = 25.4311(4) \text{ Å}, \beta = 90^{\circ}$
	$c = 14.1605(4) \text{ Å, } \gamma = 90^{\circ}$	$c = 14.1063(4) \text{ Å}, \gamma = 90^{\circ}$	$c = 14.1546(6) \text{ Å}, \gamma = 90^{\circ}$	$c = 14.1934(3) \text{ Å}, \gamma = 90^{\circ}$
Volume	994.41(6) Å ³	983.06(5) Å ³	1076.69(7) Å ³	$4591.91(14) \text{ Å}^3$
Z	4	4	4	16
Density (calculated)	3.154 g cm^{-3}	3.785 g cm ⁻³	$4.028 \mathrm{~g~cm^{-3}}$	4.327 g cm^{-3}
Absorption coefficient		16.990 mm ⁻¹	23.723 mm ⁻¹	20.076 mm ⁻¹
F(000)	864	992	1136	5120
Crystal size	$0.28 \times 0.21 \times 0.14 \text{ mm}^3$	$0.27 \times 0.21 \times 0.04 \text{ mm}^3$	$0.189 \times 0.138 \times 0.073 \text{ mm}^3$	$0.072 \times 0.052 \times 0.024 \text{ mm}^3$
θ range for data	2.877 to 33.723°	2.888 to 33.560°	2.878 to 33.766°	2.681 to 33.614°
collection				
Index ranges	$-13 \le h \le 12, -11 \le k \le 12,$	$-12 \le h \le 11, -12 \le k \le 11,$	$-13 \le h \le 12, -9 \le k \le 12,$	$-18 \le h \le 19, -38 \le k \le 36,$
	$-21 \le l \le 18$	$-21 \le l \le 20$	$-20 \le l \le 20$	$-13 \le l \le 20$
Reflections collected	7562	7530	4928	38 084
Independent	$525 [R_{\rm int} = 0.0305]$	$518 [R_{\rm int} = 0.0360]$	$553 [R_{\text{int}} = 0.0222]$	$4277 [R_{\text{int}} = 0.0325]$
reflections				
Completeness to θ =	100%	100%	100%	99.8%
25.242°				
Refinement method	Full-matrix least-squares on	Full-matrix least-squares on	Full-matrix least-squares on	
	F^2	F^2	F^2	F^2
Data/restraints/	525/1/20	518/0/18	553/0/18	4277/0/96
parameters				
Goodness-of-fit	1.152	1.144	1.112	1.047
Final R indices $[I >$	$R_{\rm obs} = 0.0139$, w $R_{\rm obs} =$	$R_{\rm obs} = 0.0177$, w $R_{\rm obs} =$	$R_{\rm obs} = 0.0156$, w $R_{\rm obs} =$	$R_{\rm obs} = 0.0229$, w $R_{\rm obs} = 0.0585$
$2\sigma(I)$	0.0306	0.0483	0.0310	
R indices [all data]	$R_{\rm all} = 0.0155$, w $R_{\rm all} = 0.0311$	$R_{\rm all} = 0.0204$, w $R_{\rm all} = 0.0495$	$R_{\rm all} = 0.0184, \text{w} R_{\rm all} = 0.0315$	$R_{\rm all} = 0.0292$, w $R_{\rm all} = 0.0611$
Extinction coefficient	0.00456(16)	0.00188(15)	0.00081(5)	N/A
Largest diff. peak and	$0.390 \text{ and } -0.336 \text{ e Å}^{-3}$	$0.780 \text{ and } -2.046 \text{ e Å}^{-3}$	$0.625 \text{ and } -0.596 \text{ e Å}^{-3}$	5.165 and –1.871 e Å ^{–3}
hole				

 $R = \sum ||F_{\rm o}| - |F_{\rm c}||/\sum |F_{\rm o}|, \ w \\ R = \{\sum [w(|F_{\rm o}|^2 - |F_{\rm c}|^2)^2]/\sum [w(|F_{\rm o}|^4)]\}^{1/2} \ \ \text{and} \ \ w = 1/[\sigma^2(F_{\rm o}^2) + (0.0094P)^2 + 3.4287P] \ \ \text{where} \ P = (F_{\rm o}^2 + 2F_{\rm c}^2)/3.4287P \}$

and by using $Olex2^{28}$ as the graphical interface. The model was refined with $ShelXL^{29}$ using least squares minimization.

Results and discussion

3.1. Synthesis

Owing to the metastability of many mixed anion compounds, reactions are often conducted at relatively lower temperature compared to more traditional solid state synthetic methods.³ Surprisingly, however, many pentanary chalcohalides, such as the related materials ABa₂MS₄X (A = Na, K, Rb, Cs; M = Sn, Ge; X = Cl, Br) were able to be synthesized at ~ 800 °C.^{24,26} Unfortunately, initial high-temperature syntheses targeting the title compounds at 800 °C produced a mixture of ABaTaS4, ACl, and trace crystals of the target phases A₂BaTaS₄Cl (A = K, Rb, Cs), suggesting metastability. To determine whether the desired phase could be isolated prior to melting, differential thermal analysis (DTA) was conducted by loading a stoichiometric reaction targeting Cs₂BaTaS₄Cl, as previously described. Upon heating the mixture, a significant exothermic event was observed, with an onset at 538.5 °C and a peak at 546.3 °C (Fig. S1). This suggests that synthesizing the material near this temperature may enable the formation of the desired phase

before decomposition occurs, which is presumed to take place upon melting. Synthesis at a lower temperature enabled the isolation of the target phases with only minor secondary phases; however, the resulting materials were obtained exclusively as polycrystalline powders. Additionally, bromine and iodine analogs were explored using both high temperature (800 °C) and lower temperature syntheses (500 °C); however, preliminary reactions only yielded a mixture of ABaTaS₄ and AX (A = K, Rb, Cs; X = Br, I).

3.2. Crystal structures of KBaTaS₄ and CsBaTaS₄

KBaTaS₄ and CsBaTaS₄ are isostructural with the previously reported RbBaTaS₄ and the average structure of KBaNbS₄, all of which crystallize in space group Pnma (Fig. 2a, Fig. S2 and Table S4–7).^{30,31} Both compounds feature isolated $[TaS_4]^{3-}$ tetrahedra, exhibiting minor distortions, which are stacked along the a-axis with alternating orientations from row to row along the b-axis (Table S7). Additionally, each structure contains one crystallographically distinct Ba atom and one distinct alkali metal atom (K or Cs), with no evidence of site mixing.

The alkali metals (K and Cs) are each 10-coordinated, surrounded by five symmetry-related [TaS₄]³⁻ tetrahedra (Fig. 2b and c). In KBaTaS₄, eight of the K-S bond lengths range from

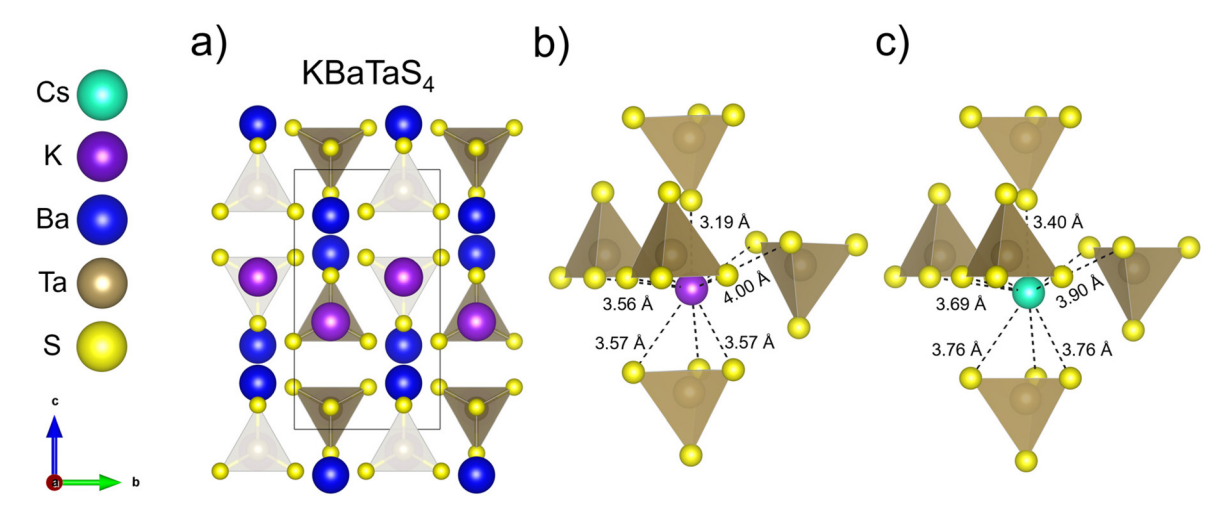


Fig. 2 Crystal structure of (a) KBaTaS₄ viewed down the *a*-axis highlighting TaS₄ tetrahedra, which are also found in the mixed-anion material. Moving from KBaTaS₄ to CsBaTaS₄, there are slightly greater distortions in the (b) K⁺ coordination environment compared to the (c) Cs⁺ coordination environment

3.1923(7) Å to 3.7576(19) Å, while in CsBaTaS₄, the ten Cs–S bonds range from 3.4010(19) Å to 3.9046(11) Å. The remaining two K–S bonds (associated with one tetrahedron) are significantly elongated at 4.0048(17) Å each, well beyond the sum of the ionic radii for a coordination number (CN) of 10 (3.43 Å). In contrast, Ba is 9-coordinated, surrounded by six symmetry-related [TaS₄]^{3–} tetrahedra. The Ba–S bond lengths range from 3.2066(13) Å to 3.7177(5) Å in KBaTaS₄ and from 2.25 Å to 3.7720(6) Å in CsBaTaS₄.

At room temperature, no evidence of any structural modulation was observed in any of the compounds, in contrast to the previously reported behavior in KBaNbS₄ where slight tilting of the NbS₄ tetrahedra and K and Ba displacements led to the modulation.³⁰ Additional low-temperature screening to investigate potential ordering was not conducted.

3.3. Crystal structures of K₂BaTaS₄Cl, Rb₂BaTaS₄Cl, and K₂BaNbS₄Cl

K₂BaTaS₄Cl, Rb₂BaTaS₄Cl, and K₂BaNbS₄Cl are isostructural with previously reported mixed-anion compounds such as NaBa₂SnS₄Cl, KBa₂SnS₄Cl, Ba₃InS₄Cl, and Ba₃InSe₄Cl, all of which adopt the Cs₃CoCl₅ structure type. 19,22,24 These materials can alternatively also be described within the K3SO4F structure-type, which emphasizes the additional anion ordering present. As is the case with both the Cs₃CoCl₅ and K₃SO₄F structure types, K2BaTaS4Cl, Rb2BaTaS4Cl and K2BaNbS4Cl all crystallize in the tetragonal space group, I4/mcm, and can be seen as the MV analogues of the previously reported mixedanion compounds, Ba₃InS₄Cl and KBa₂SnS₄Cl (Fig. 3 and Table 1). 22,24 As the oxidation state of the metal increases from In^{III} to Sn^{IV} and ultimately to Ta^V, substitution of a Ba²⁺ cation with a monovalent alkali metal provides charge compensation for the additional positive charge, while preserving the overall structural framework with minimal distortions.

There are several ways to describe the structure of these materials. For example, Li et al. describe these compounds as being arranged in two layers stacked along the c-axis.²⁴ Using this explanation, in one layer there are 8-coordinated Ba/A (A = K, Rb) bound to Cl and S along with octahedral Cl atoms, we can call this layer A, followed by a layer composed of MS₄ tetrahedra and 10-coordinated Ba/A atoms, which we can call layer B (Fig. 4a). These two kinds of planes are stacked alternately to build up the complete 3-dimensional structure. Alternatively, these materials can be viewed as an ionic cage of alkali and alkaline earth metal cations surrounding MS₄ tetrahedron, similar to that of an anti-perovskite in the one-tilt system $a^{\circ}a^{\circ}$ $c^{-.32-35}$ For the M^{5+} case, this results in the formation of an ionic cage of octahedral, $[A_2BaCl]^{3+}$, connected by $[MS_4]^{3-}$ tetrahedra, which are additionally held in place through A-S and Ba-S bonds. This explanation also helps us better understand how these mixed-anion compounds relate to their degradation products, ABaTaS₄ and ACl (Fig. 4b and Fig. S2).

Although structurally very similar, the three compounds exhibit subtle differences in the ordering of K/Rb and Ba cations. In K₂BaTaS₄Cl, the alkali metal K and Ba occupy distinct Wyckoff sites and are thus crystallographically independent. In contrast, K₂BaNbS₄Cl and Rb₂BaTaS₄Cl show varying degrees of cation mixing between the alkali metal and alkali earth metal sites. While Rb₂BaTaS₄Cl has a constant distribution of 2/3 Rb and 1/3 Ba in both *layer A* and *layer B*, in K₂BaNbS₄Cl *layer B* remains Ba rich, 88% Ba and 12% K, while *layer A* remains K rich, 94% K and 6% Ba (Fig. S3). This trend shows a dependence on the size of the metal tetrahedra in relation to the degree of alkali/alkali-earth metal ordering.

Finally, a challenge in the structural refinement arises from the difficulty in distinguishing Cl⁻ and S²⁻ atoms crystallographically due to their similar X-ray scattering factors. To address this issue, anions assignments were guided by hardsoft acid-base theory, consistent with approaches used in

Paper

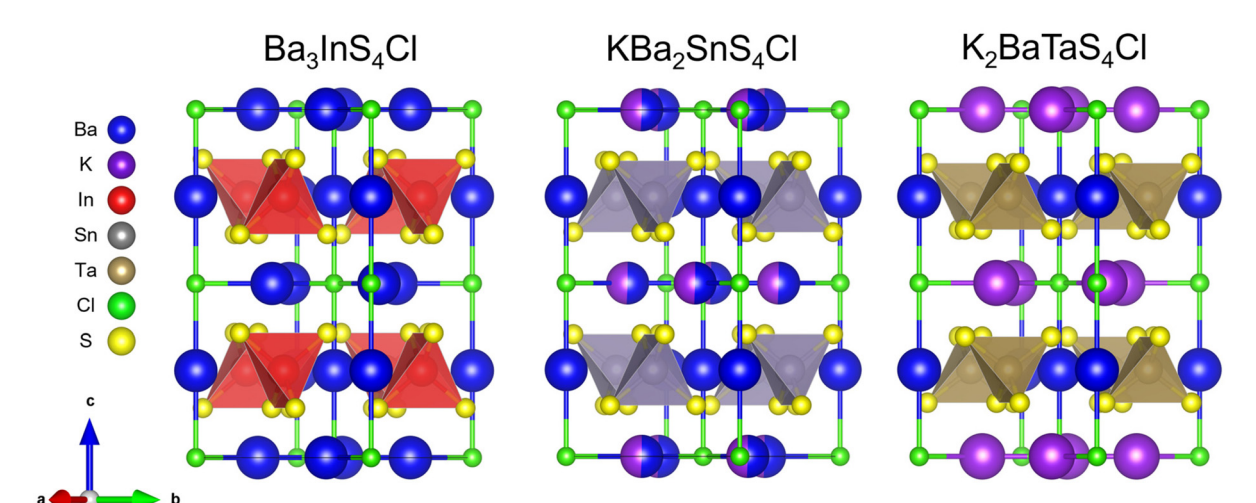


Fig. 3 Crystal structure of $A_xBa_{3-x}M^{(III+x)}S_4Cl$ compounds. As the oxidation state of the metal increases from In^{3+} to Ta^{5+} , additional alkali metal cations are introduced to maintain charge balance, compensating for the higher positively charged metal. Alkali/alkali earth metal-sulfur bonds are not drawn to better distinguish the $[TaS_4]^{3-}$ tetrahedron.

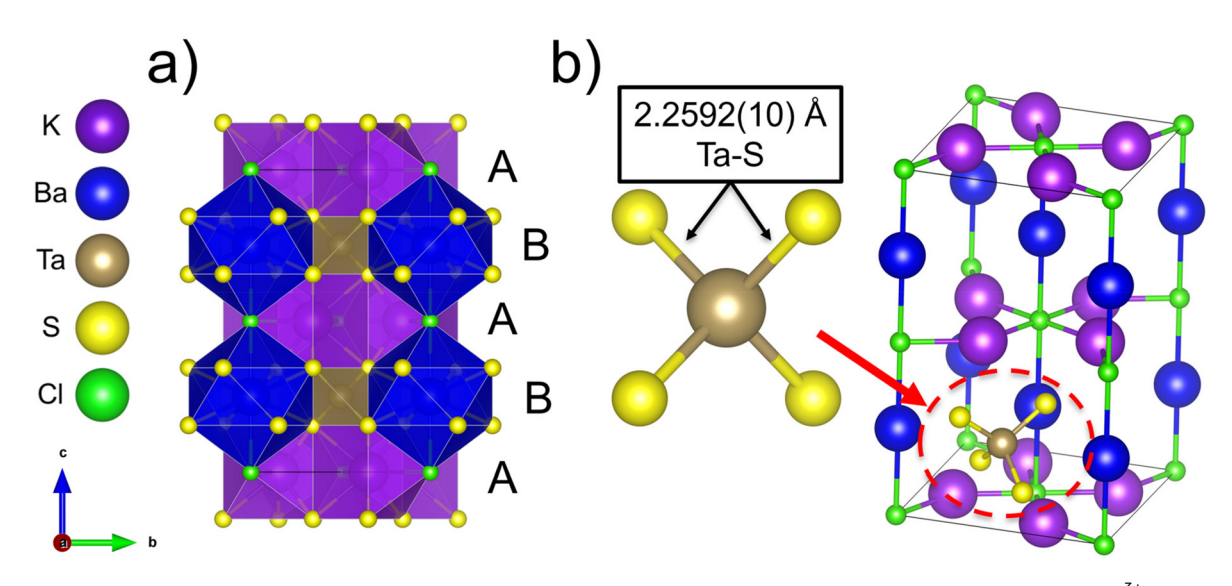


Fig. 4 Crystal structure of K_2BaTaS_4Cl (a) down the a-axis highlighting the layered stacking sequence as well as the (b) $[K_2BaCl]^{3+}$ ionic framework with a singular undistorted $[TaS_4]^{3-}$ unit within the cage.

related compounds. Given that S^{2-} is a much softer acid compared to Cl⁻, S was assigned to covalently bind to the Nb/Ta atoms, while Cl was assigned to exclusively bond with the harder A/Ba (A = K, Rb), matching Ba₃InS₄Cl and KBa₂SnS₄Cl. Additionally, the tetrahedral Nb-S and Ta-S bond distances of ~2.26 Å are identical to previously reported NbS₄ and TaS₄ tetrahedra *e.g.* A₃(Nb,Ta)S₄ (A = K, Rb, Cs) while no tetrahedral Nb/Ta-Cl species are reported with Nb/Ta compounds primarily forming octahedra when coordinating with Cl.

3.4. Crystal structures of Cs₂BaTaS₄Cl

 Cs_2BaTaS_4Cl adopts a structure similar to its K and Rb analogues, however, it uniquely forms a supercell, resulting in a $\sqrt{2}$ expansion along the a-axis and a $2\sqrt{2}$ expansion along the

b-axis. This distortion arises from preferential site ordering between Ba²⁺ and Cs⁺, leading to a more pronounced rearrangement of the ionic framework than observed in any other compounds (Fig. 5, 6 and Table 1). The effect of this site preference can be most clearly seen when observing the Cl coordination environment. In the typical Cs₃CoCl₅ structure, every Cl atom forms an undistorted octahedron that is corner sharing. In contrast, for Cs₂BaTaS₄Cl, the Cl atoms adopt both an undistorted octahedral coordination and a distorted one, which can be seen as alternating 2-tilt and 1-tilt regions when viewed as an anti-perovskite like structure (Fig. 7). This is caused by Cs and Ba site ordering within *layer A* of the structure, where a Cl⁻ anion coordinates to both a distinct Cs and Ba rather than being randomly mixed or only coordinated to

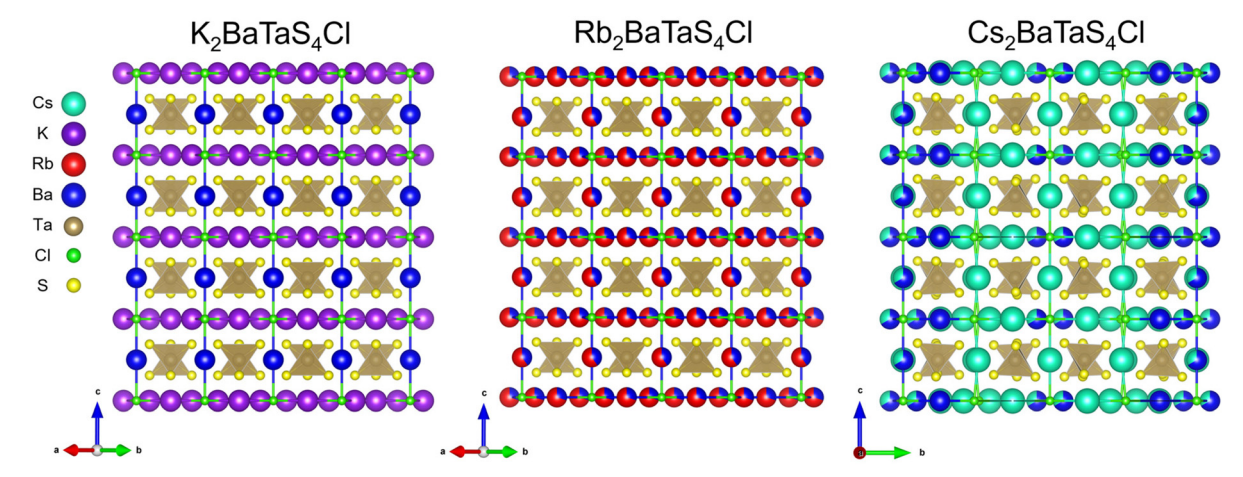


Fig. 5 Crystal structures of K_2BaTaS_4Cl , Rb_2BaTaS_4Cl , and Cs_2BaTaS_4Cl showing additional cation mixing as the alkali metal sizes increase. Alkali/alkali earth metal-sulfur bonds not drawn to better distinguish TaS_4 tetrahedron.

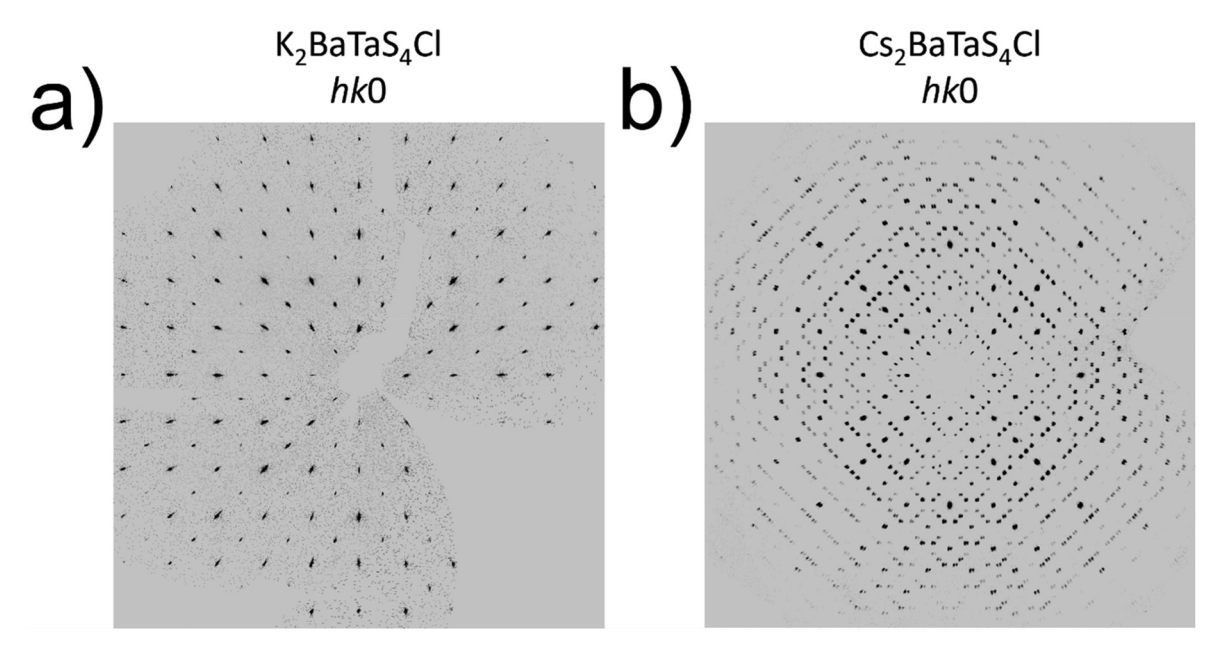


Fig. 6 Synthetic precession image of reciprocal space when viewed down the c-axis (hk0 plane) for K_2BaTaS_4Cl and Cs_2BaTaS_4Cl . Cs_2BaTaS_4Cl shows additional satellite reflections along the a and b axes when compared to K_2BaTaS_4Cl , resulting in a $\sqrt{2}$ expansion along the a-axis and a $2\sqrt{2}$ expansion along the b-axis.

an alkali metal. As Ba²⁺ is more electronegative than Cs⁺, this results in the Cs-rich octahedra becoming distorted as it is pulled towards Ba²⁺.

As Cs and Ba cations can be difficult to distinguish crystal-lographically due to their similar X-ray scattering factors, comparison of coordination environments and bond lengths were used to distinguish between the two. Thus, to determine the proper assignments for each crystallographic site, bond valence sum (BVS) analysis was used to determine which sites were Cs, which sites were Ba, and which sites were mixed (Table 2).³⁶ In conducting these calculations, it was observed that one site was deemed to be only Ba, showing a BVS of ~2, while four other sites were assigned only Cs as they all show a

BVS \sim 1. This left two sites that showed values between 1 and 2, independent of which element was assigned to these sites. We thus concluded that these sites were mixed occupancy, making them 1/3 Cs and 2/3 Ba to maintain charge neutrality.

3.5. Air stability and solubility

Air stability was measured on all samples after 3 weeks, where PXRD was monitored on samples left out in ambient conditions. It was observed that K₂BaTaS₄Cl, K₂BaNbS₄Cl Rb₂BaTaS₄Cl remained stable over 1 month in ambient conditions, as no clear change in the PXRD was observed, while after a month, Cs₂BaTaS₄Cl entirely degraded (Fig. S4).

Paper

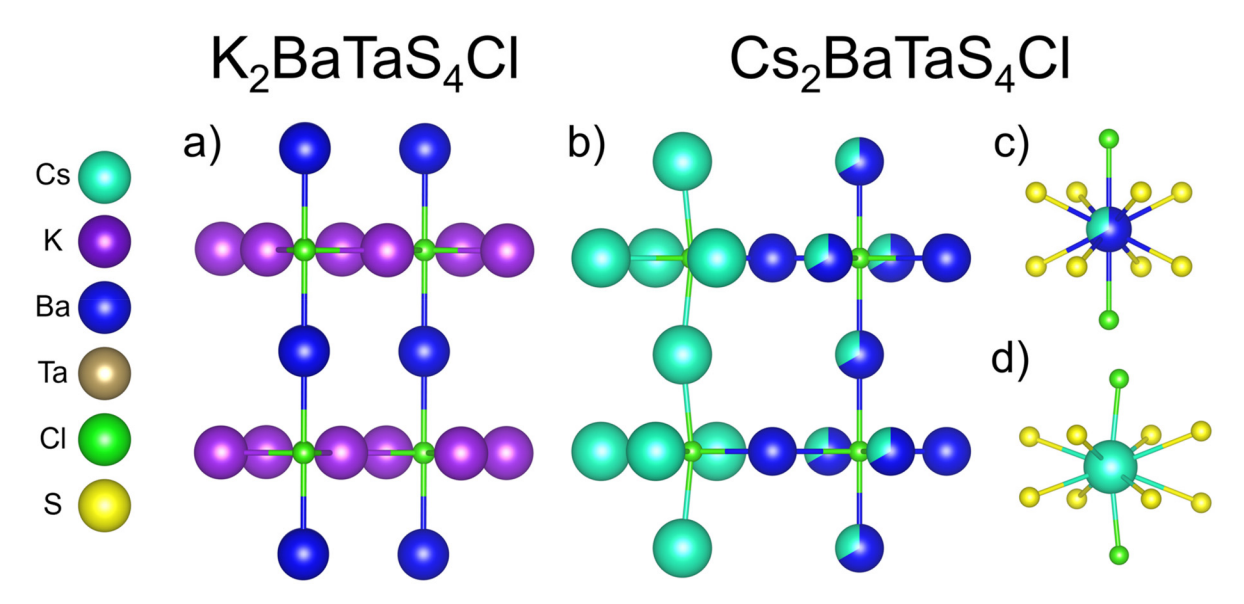


Fig. 7 Cl coordination environments for (a) K_2BaTaS_4Cl and (b) Cs_2BaTaS_4Cl alongside (c and d) the *layer A* alkali metal coordination environments for Cs_2BaTaS_4Cl . K_2BaTaS_4Cl has only undistorted Cl octahedra, while Cs_2BaTaS_4Cl shows an alternating pattern of undistorted and distorted octahedra, resulting from enhanced cation ordering and structural modulation within the layers.

Table 2 Bond valence sum (BVS) sum calculations for Cs and Ba in Cs_2BaTaS_4Cl . BVS for both Ba and Cs are showed for mixed sites

Atom	Bond valence sum
Ba1/Cs1	1.60/2.21
Ba2/Cs2	1.71/2.35
Ba3	2.04
Cs3	1.14
Cs4	1.13
Cs5	0.94
Cs5 Cs6 ^a	1.28 (0.80)

^a BVS in parenthesis are calculated assuming Ba as the atom.

Additionally, the solubility of K₂BaTaS₄Cl was tested in water (H₂O), dimethylformamide (DMF), acetonitrile (ACN), and ethanol (EtOH). In the protic solvents, H₂O and EtOH, all materials instantly degraded, which was observed with H₂S formation, resulting in bubbling and the solvent turning yellow. While the material remained stable in the aprotic solvents, DMF and ACN, significant solubility was not observed (Fig. S5).

3.6. Thermal stability

Thermal stability was investigated using differential thermal analysis (DTA) and PXRD before and after thermal cycling (DTA methods can be found in the SI). DTA revealed endothermic events presumed to correspond to melting at 680 °C, 618 °C, and 643 °C for K₂BaTaS₄Cl, Rb₂BaTaS₄Cl, and K₂BaNbS₄Cl, respectively. Interestingly, Cs₂BaTaS₄Cl reproducibly showed two endothermic events around the point of melting at 594 °C and 647 °C on heating. Upon cooling, K₂BaTaS₄Cl, Cs₂BaTaS₄Cl, and K₂BaNbS₄Cl all showed multiple exothermic events presumably corresponding to multiple

species recrystallizing, while Rb₂BaTaS₄Cl showed a singular event at 586 °C (Fig. S6). While the majority of related compounds in the A_xBa_{3-x}M^{III+x}Q₄X family have been found to be thermally stable, which can be deduced from the high temperature synthetic methods used to obtain each, PXRD analysis confirmed that all four MV compounds melt and degrade to ABaMS₄ and ACl products, potentially due to the high formation energy of the single anion phase, ABaMS₄ (Fig. S7). The extent of decomposition additionally varies among the samples: K2BaTaS4Cl, Rb2BaTaS4Cl, and K2BaNbS4Cl remain mostly intact with the addition of only a few minor impurity peaks after melting. In contrast, Cs2BaTaS4Cl degrades completely to CsBaTaS4 and CsCl upon melting. We understand this as a result of the increased softness of the alkali metal as it gets larger, which results in a weaker bond with the hard Cl anion. Thus, resulting in greater degradation upon heating and a lower melting temperature.

3.7. Optical properties

Diffuse reflectance (DR) UV-Vis spectroscopy was conducted on all materials post-washing to measure each material's bandgap (Diffuse reflectance UV-Vis spectroscopy methods can be found in the SI). For the Ta based mixed-anion materials, DR UV-Vis showed bandgaps of 3.01(5) eV, 2.97(5) eV, and 2.97(5) eV for K₂BaTaS₄Cl, Rb₂BaTaS₄Cl, and Cs₂BaTaS₄Cl, showing them all to be within error of each other and consistent with their white color. Upon replacing Ta with Nb in K₂BaNbS₄Cl, the bandgap then subsequently decreases to 2.46 (5) eV, which matches the material's bright yellow color (Fig. 8b). Upon removing an equivalent of ACl yielding ABaTaS₄, the bandgap essentially remains unchanged, showing bandgaps of 2.93(5) eV, 3.00(5) eV and 2.99(5) eV for KBaTaS₄, RbBaTaS₄, and CsBaTaS₄, respectively, which are

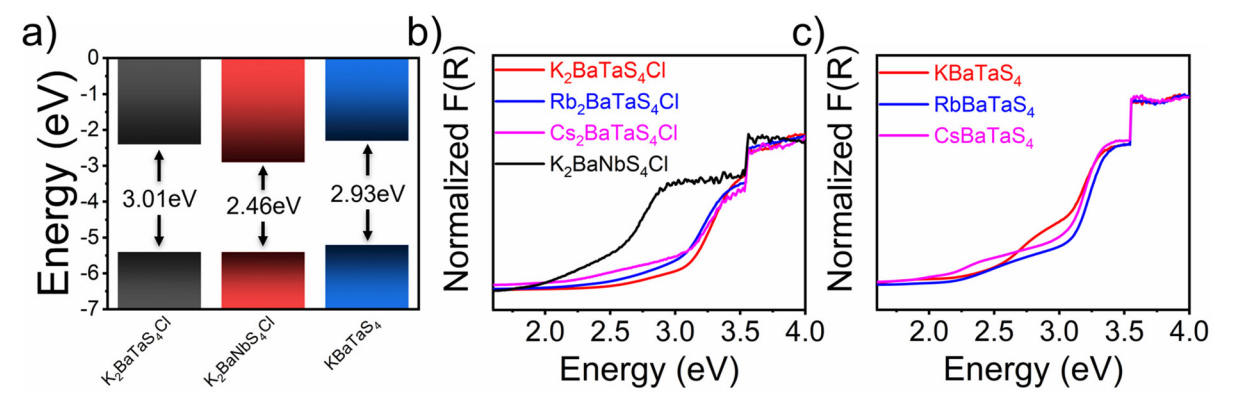
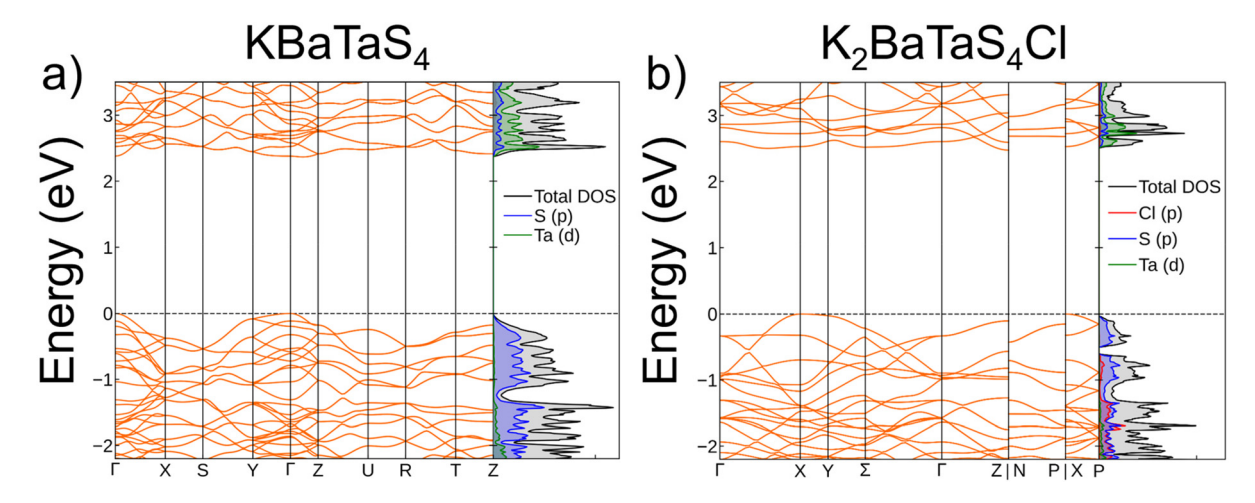


Fig. 8 (a) Position of the CBM and VBM relative to the free electron comparing K2BaTaS4Cl, K2BaNbS4Cl and KBaTaS4, and the optical diffuse reflectance spectra of (b) A_2BaMS_4Cl and (c) $ABaTaS_4$ (A = K, Rb, Cs; M = Nb, Ta) highlighting the extrapolated band edges. The abrupt increase in F(R) at ~3.55 eV is an artifact from the instrument caused by a change in the detector.

within the error of the measurement with their respective mixed-anion materials (Fig. 8c). This observation is surprising, the incorporation of halide species often results in an increase in the band gap of heteroanionic materials as is the case in the related Sn compounds Ba₂SnSe₄ and KBa₂SnSe₄Cl, which show a ~0.6eV increase in the band gap upon the incorporation of KCl.²⁵ The minimal change in the optical properties for either structure type suggests the HOMO and LUMO are dominated by sulfur and Ta/Nb states with minimal to no influence from the alkali metal and Cl states.

A better understanding of the electronic structures can be obtained by using photoemission yield spectroscopy in air (PYSA) to determine each material's first ionization energy (PYSA methods can be found in the SI). Combining bandgap measurements alongside measured ionization energies allows us to elucidate each material's conduction band minimum (CBM) and valence band maximum (VBM) relative to the energy of a free electron by subtracting the bandgap from the ionization energy (Fig. S8, 9 and Fig. 8a). This shows that all the chalcohalide materials have similar VBMs while the single anion materials have a VBM shifted to higher energy with respect to their mixed-anion counterparts. As the K2BaNbS4Cl has a lower bandgap than the Ta based materials while also having an identical VBM, we can conclude that the smaller bandgap is due to a lowering of the CBM (Fig. 8a), which is governed by the Nb/Ta d orbitals at the CBM.

These findings are all corroborated with DFT-calculated band structures comparing K2BaTaS4Cl to KBaTaS4 (Fig. 9). The projected density of states (pDOS) reveals in both compounds the dominance of S (p) states at the Fermi level, with the empty Ta (d) orbitals forming the first conduction band, consistent with experiment. Additionally, our simulations indicate that the mixed-anion compound has a slight increase of 0.26 eV in the bandgap, 2.43 eV for KBaTaS₄ compared to 2.69 eV for K2BaTaS4Cl. The calculations additionally show that KBaTaS4 has a direct bandgap with both the VBM and CBM located at Γ . In contrast, the mixed-anion compound K₂BaTaS₄Cl exhibits a significant change in electronic structure, displaying an indirect bandgap with the VBM at X and the CBM at Z.



Combined DFT electronic band structures and density of states (DOS) for (a) KBaTaS₄ and (b) K₂BaTaS₄Cl.

4. Conclusions

Paper

The discovery of novel mixed-anion materials remains a significant challenge, largely due to the thermodynamic preference for forming more stable single-anion phases. By building prior work with compounds of the formula A_xBa_{3-x}M^{III+x}Q₄X, and employing low-temperature synthesis, successfully prepared four novel chalcohalides, K₂BaTaS₄Cl, Rb₂BaTaS₄Cl, Cs₂BaTaS₄Cl and K₂BaNbS₄Cl, by incorporating a pentavalent transition metal. These results demonstrate that the A/Ba ratio in this structural family can be tuned to accommodate higher metal oxidation states. We further show that alkali metal size significantly impacts cation ordering, with increasing size leading to greater A/Ba mixing culminating in the emergence of a superstructure for Cs₂BaTaS₄Cl. Despite these structural variations, the electronic properties remain largely unchanged across the series, with the valence and conduction band edges dominated by chalcogen and transition metal states, as supported by DFT, experimental band gaps, and PYSA measurements. Together, these findings underscore how subtle changes in composition and size affect structure in these mixed-anion phases, while offering a framework for designing new mixed-anion materials.

Conflicts of interest

The authors declare no competing financial interest.

Data availability

Crystallographic tables and other data supporting this article are also provided in the SI: additional experimental details and methods, DTA reaction of Cs_2BaTaS_4Cl , crystal structure figure of $CsBaTaS_4$ and K_2BaNbS_4Cl , air stability and solvent stability tests, DTA graphs of K_2BaTaS_4Cl , Rb_2BaTaS_4Cl , Cs_2BaTaS_4Cl , and K_2BaNbS_4Cl as well as their PXRDs before and after heating, PYSA graphs, and additional crystallographic tables for all the reported compounds. See DOI: https://doi.org/10.1039/d5dt01676b.

CCDC 2472244–2472250 contain the supplementary crystallographic data for this paper. $^{\rm 37a-g}$

Acknowledgements

T. S. I. and M. G. K. acknowledge the financial support of the National Science Foundation (NSF) under award DMR-2305731. Computational work by S. S. N. and J. M. R. was supported by NSF under award DMR-2413680. This work made use of the IMSERC (RRID:SCR_017874) Crystallography facility at Northwestern University, which has received support from the Soft and Hybrid Nanotechnology Experimental (SHyNE) Resource (NSF ECCS-2025633), and Northwestern University.

References

- 1 A. Tassanov, H. Lee, Y. Xia and J. M. Hodges, *J. Am. Chem. Soc.*, 2024, **146**, 32627–32639.
- 2 B. M. Oxley, J. B. Cho, A. K. Iyer, M. J. Waters, J. He, N. C. Smith, C. Wolverton, V. Gopalan, J. M. Rondinelli, J. I. Jang and M. G. Kanatzidis, *J. Am. Chem. Soc.*, 2022, 144, 13903–13912.
- 3 H. Kageyama, H. Ogino, T. Zhu and T. Hasegawa, *Mixed-Anion Compounds*, Royal Society of Chemistry, 2024.
- 4 K. Maeda, F. Takeiri, G. Kobayashi, S. Matsuishi, H. Ogino, S. Ida, T. Mori, Y. Uchimoto, S. Tanabe and T. Hasegawa, *Bull. Chem. Soc. Jpn.*, 2022, **95**, 26–37.
- 5 Y. Zhang, H. Wu, Z. Hu and H. Yu, *Chem. Eur. J.*, 2023, **29**, e202203597.
- 6 J. K. Harada, N. Charles, K. R. Poeppelmeier and J. M. Rondinelli, *Adv. Mater.*, 2019, 31, 1805295.
- 7 M. Valldor, Inorganics, 2016, 4, 23.
- 8 H. Kageyama, K. Hayashi, K. Maeda, J. P. Attfield, Z. Hiroi, J. M. Rondinelli and K. R. Poeppelmeier, *Nat. Commun.*, 2018, **9**, 772.
- 9 Y.-Y. Li, W.-J. Wang, H. Wang, H. Lin and L.-M. Wu, Cryst. Growth Des., 2019, 19, 4172–4192.
- 10 R. McClain, C. C. Laing, J. Shen, C. Wolverton and M. G. Kanatzidis, *Inorg. Chem.*, 2022, **61**, 9040–9046.
- 11 S. Yadav, G. Panigrahi, M. K. Niranjan and J. Prakash, J. Solid State Chem., 2023, 323, 124028.
- 12 S. Tippireddy, D. S. Prem Kumar, S. Das and R. C. Mallik, ACS Appl. Energy Mater., 2021, 4, 2022–2040.
- 13 J. Cui, C. Li and F. Zhang, ChemSusChem, 2019, 12, 1872– 1888.
- 14 Z.-Z. Luo, H. Zhao, W. Cai, S. Shahabfar, J. Li, S. Cai, J. Berg, T. Bhowmick, J.-K. Bao and S. Hao, *J. Am. Chem. Soc.*, 2025, 147, 6753–6762.
- 15 C. C. Laing, D. Kim, J. Park, J. Shen, I. Hadar, J. M. Hoffman, J. He, B. Shin, C. Wolverton and M. G. Kanatzidis, *Nat. Mater.*, 2024, 23, 230–236.
- 16 X. Zhou, C. D. Malliakas, A. A. Yakovenko, B. Wilfong, S. G. Wang, Y.-S. Chen, L. Yu, J. Wen, M. Balasubramanian and H.-H. Wang, *Nat. Synth.*, 2022, 1, 729–737.
- 17 W. Yin, A. K. Iyer, W. Xing, B. Kang and A. Mar, *J. Solid State Chem.*, 2020, **284**, 121189.
- 18 A. Tudi, S. Han, A. Abudurusuli, H. Yu, Z. Yang and S. Pan, *Dalton Trans.*, 2019, **48**, 12713–12719.
- 19 K. Feng, W. Yin, Z. Lin, J. Yao and Y. Wu, *Inorg. Chem.*, 2013, 52, 11503–11508.
- 20 X. Li, C. Li, L. Kang, Y. Wu, Z. Lin, J. Yao and Y. Wu, Eur. J. Inorg. Chem., 2016, 2016, 1359–1363.
- Zi. J. Hong, K. Liu, J.-Q. He, H. Wu, Q.-Z. Huang, J.-H. Lin,
 Z.-Y. Lu and F.-Q. Huang, Sci. Rep., 2015, 5, 15910.
- 22 M.-Y. Pan, S.-Q. Xia, X.-C. Liu and X.-T. Tao, J. Solid State Chem., 2014, 219, 74–79.
- 23 M.-Y. Li, Y.-X. Zhang, H. Lin, Z. Ma, X.-T. Wu and Q.-L. Zhu, *Dalton Trans.*, 2019, **48**, 17588–17593.
- 24 C. Li, K. Feng, H. Tu, J. Yao and Y. Wu, *J. Solid State Chem.*, 2015, 227, 104–109.

25 X. Meng, J. Shi, M. Sun and J. Yao, *Cryst. Growth Des.*, 2023, 23, 5409–5413.

Dalton Transactions

- 26 Y. Chu, K. Wu, X. Su, J. Han, Z. Yang and S. Pan, *Inorg. Chem.*, 2018, 57, 11310–11313.
- 27 G. M. Sheldrick, *Acta Crystallogr.*, *Sect. A:Found. Adv.*, 2015, 71, 3–8.
- 28 O. V. Dolomanov, L. J. Bourhis, R. J. Gildea, J. A. K. Howard and H. Puschmann, *J. Appl. Crystallogr.*, 2009, **42**, 339–341.
- 29 G. M. Sheldrick, Acta Crystallogr., Sect. C:Struct. Chem., 2015, 71, 3-8.
- 30 Y. Wu, T. Doert and W. Bensch, *Z. Anorg. Allg. Chem.*, 2005, **631**, 3019–3024.
- 31 Y. Wu and W. Bensch, Z. Naturforsch., B:J. Chem. Sci., 2010, 65, 1219–1228.
- 32 A. M. Glazer, Struct. Sci., 1972, 28, 3384-3392.
- 33 P. M. Woodward, Struct. Sci., 1997, 53, 32-43.
- 34 P. M. Woodward, Struct. Sci., 1997, 53, 44-66.
- 35 C. J. Howard and H. T. Stokes, Struct. Sci., 1998, 54, 782-789.
- 36 I. D. Brown, *The chemical bond in inorganic chemistry: the bond valence model*, Oxford university press, 2016.
- 37 (a) T. S. Ie, S. S. Nathan, J. M. Rondinelli, and M. G. Kanatzidis, CCDC 2472244 (Rb₂BaTaS₄Cl):

Experimental Crystal Structure Determination, 2025, DOI: 10.5517/ccdc.csd.cc2nzkt1; (b) T. S. Ie, S. S. Nathan, J. M. Rondinelli, and M. G. Kanatzidis, CCDC 2472245 (CsBaTaS₄): Experimental Crystal Structure Determination, 2025, DOI: 10.5517/ccdc.csd.cc2nzkv2; (c) T. S. Ie, S. S. Nathan, J. M. Rondinelli, and M. G. Kanatzidis, CCDC 2472246 (K₂BaNbS₄Cl): Experimental Crystal Structure Determination, 2025, DOI: 10.5517/ccdc.csd.cc2nzkw3; (d) T. S. Ie, S. S. Nathan, J. M. Rondinelli, and G. Kanatzidis, CCDC 2472247 (K_2BaTaS_4Cl): Experimental Crystal Structure Determination, 2025, DOI: 10.5517/ccdc.csd.cc2nzkx4; (e) T. S. Ie, S. S. Nathan, J. M. Rondinelli, and M. G. Kanatzidis, CCDC 2472248 (RbBaTaS₄): Experimental Crystal Structure Determination, 2025, DOI: 10.5517/ccdc.csd.cc2nzky5; (f) T. S. Ie, S. S. Nathan, J. M. Rondinelli, and M. G. Kanatzidis, CCDC 2472249 (KBaTaS₄): Experimental Crystal Structure Determination, 2025, DOI: 10.5517/ccdc.csd.cc2nzkz6; (g) T. S. Ie, S. S. Nathan, J. M. Rondinelli, and G. Kanatzidis, CCDC 2472250 (Cs₂BaTaS₄Cl): Experimental Crystal Structure Determination, 2025, DOI: 10.5517/ccdc.csd.cc2nzl08.